

SearchMorph: Multi-scale Correlation Iterative Network for Deformable Registration

Xiao Fan, Shuxin Zhuang, Zhemin Zhuang, Shunmin Qiu, Alex Noel Joseph Raj and Yibiao Rong

Abstract—Deformable image registration gives dynamic information about the image. It is of great importance in medical image analysis. In the image registration, we found two issues to be solved. The first is the issue of model generality. To our knowledge, there is not yet a model for both single- and multi-temporal phases. The second is that most iteration-based deep learning models suffer from excessive smoothing of the deformation field. We propose an unsupervised multi-scale correlation iterative registration network (SearchMorph) with the following advantages. (1) The proposed method allows accurate registration of large and small deformations. (2) The images registered by the proposed method are better for detail and can be further optimized for detail when adding iteration. (3) This network uses iteration to generate benefits while maintaining the smoothness of the deformation field. (4) The model can adapt single-temporal MR images of the brain and multi-temporal echocardiographic sequences without adding restrictions. Our method achieves higher registration accuracy and lower folding point ratios than other methods.

Index Terms—unsupervised registration, optical flow, medical imaging, tracking

I. INTRODUCTION

Deformable image registration is of great importance in medical image processing and analysis. It maps a moving image onto a fixed image by finding a spatial transformation. Traditional methods solve the image registration for a strategy of maximum or minimizing objective function [5]–[9]. These often require heavy calculations and result in a lengthy registration process. Moreover, the traditional approach requires the design of different objective functions to readapt different datasets, resulting in weak generalization capabilities.

With the event of deep learning (DL), the application of DL in image registration has become a hot research topic. Deep learning image registration shows higher performance than traditional image registration, which solves the issues of a lengthy registration process and weak generalization ability. Early supervised methods [10]–[13] use ground-truth

deformation field as label for image registration. However, the ground-truth deformation field is hard to obtain, so supervised methods are challenging to apply.

Unsupervised registration networks will carry out end-to-end learning without labels, overcoming the dependence of supervised methods on labels. Unsupervised learning also currently faces several limitations. For example, most models based on the VoxelMorph framework directly predict the deformation field by feature map, making it challenging to estimate large deformation. [20] adopted the strategy of recursive cascaded learning deformation field step by step, improving the model's registration ability for large deformation. This strategy is feasible. Since recursive cascade does not strengthen the correlation between features, the deformation field becomes less natural while improving the registration performance. In multi-temporal image registration, [17] proposes a joint learning framework for multi-temporal images, which achieves high scores on short-axis MR sequences by simultaneously optimizing segmentation and motion estimation branches. However, this method is challenging to register low signal-to-noise ratio images such as ultrasound images. Moreover, the joint learning framework can not estimate the motion accurately without the segmentation branch.

In this work, we proposed an unsupervised multi-scale correlation iterative registration network (SearchMorph). Our proposed model allows accurate registration of single-temporal brain MR images and accurate motion estimation of multi-temporal echocardiograms without adding any constraints.

The main contributions of our work are summarized as follows:

- We address a correlation layer that calculates the cost volume for the features. The cost volume stores information about the correlation between features. We also constructed a multi-scale relevance pyramid by pooling the latter two dimensions of the cost volume. The correlation pyramid provides the network with information on both small and large deformations, enhancing the network's ability to register multi-scale deformations. The correlation pyramid also provides reference information to the network when registering low signal-to-noise images.
- We design a deformation field iterator using GRU as the iteration module. GRU enables the network to register multiple times in a single prediction iteratively. The point to be registered gradually converge to a definite point by iteration. Based on this design, the model-registered image has better detail, and the deformation field is more realistic. GRU refines the deformation field without

Xiao Fan is with the Shantou University, Shantou 515063, China (e-mail: 20xfan1@stu.edu.cn).

Shuxin Zhuang and Alex Noel Joseph Raj are with the Shantou University, Shantou 515063, China (e-mail: sxzhuang@stu.edu.cn; jalexnoel@stu.edu.cn).

Shunmin Qiu is with the First Affiliated Hospital of Shantou University, Shantou 515041, China (e-mail: shunmqiu@163.com).

Yibiao Rong is with the Shantou University, Shantou 515063, China (e-mail: ybrong@stu.edu.cn).

Corresponding author: Zhemin Zhuang is with the Shantou University, Shantou 515063, China (e-mail: zmzhuang@stu.edu.cn).

This work was supported by the National Natural Science Foundation of China under Grant 82071992, Basic and Applied Basic Research Foundation of Guangdong Province under Grant 2020B1515120061, the Guangdong Province University Priority Field (Artificial Intelligence) Project under Grant 2019KZDZX1013.

using more parameters, helping the network learn helpful information in each iteration.

- We also propose a search module for deformation field iterators. The function of the search module is to search the correlation pyramid with a fixed radius to find the best registration point. This module makes the search for registration points regular and suppresses voxel point folding. Moreover, this strategy ensures that the search range is small to large, improving the performance of model registration details and large deformable.

II. RELATED WORK

A. Traditional image registration

Classical medical alignment methods are usually performed using an iterative optimization strategy. These methods find the spatial transformation between two images and align two or more images.

In the deformable image registration, [1]–[3] proposes elastic and B-splines models for the alignment of multiple feature points of the image. The diffeomorphic transformation solves the problem of overlap after the alignment of pixel points. The Symmetric image normalization method (SyN) [9] preserves the binary transformation of the topology. [4] proposes the large displacement diffeomorphic metric mapping (LDDMM) to solve large displacement alignments. [5] proposes that the RDMM model tracks deformation through a special regularizer. While these methods have met with some success, the need to create a new objective function for each pair of images for alignment mapping is inefficient and time-consuming.

B. Deep learning for image registration

Deep learning-based image registration methods have been a hot topic of research in recent years. Deep learning methods have short registration times and, due to their inductive nature, can be used to register multiple images with just one model. Most people try to do supervised learning using segmented labels or synthetic deformation fields based on ground truth, etc. The registration performance of these methods is dependent on the quality of the labels and synthetic deformation fields, making the information learned by the model limiting.

The unsupervised method overcomes the reliance of the supervised on ground truth. Earliest, JaderBerg *et al.* proposed the spatial transformer network (STN) [14]. STN automatically performs affine transformations on the input data without learning any parameters and has subsequently become an important part of the unsupervised framework. On this basis, Vos *et al.* uses the properties of the STN for unsupervised non-rigid body registration [15]. VoxelMorph, proposed by Balakrishnan *et al.* enables unsupervised registration of brain MR data. Xu *et al.* proposed a recursive cascade network VTN to improve the performance of unsupervised registration [20]. VTN allows the model to progressively learn the deformable field by warping the image several times and thus registering it with the fixed image. Fan *et al.* used a discriminant instead of a loss function for registration [21]. Zhu *et al.* used image pyramids for registration to register echocardiograms [16]. Qin

et al. proposed a joint learning network [17] that registers time-series images by optimally segmenting branches and motion estimation. Kim *et al.* used cycle consistency to bring the images closer to diffeomorphic homogeneity [22]. Chen *et al.* used the transformer encoder instead of the CNN [19].

C. Optical Flow Estimation

Optical flow estimation is related to image registration, and they correlate the parts of the two images that change. The difference is that optical flow often estimates the motion of a rigid object, whereas registration often estimates the deformation of a non-rigid object. We can use the idea of motion estimation for multi-temporal alignment, which means that each pixel point is tracked, thus improving the performance of the multi-temporal registration.

Dosovitskiy *et al.* proposed FlowNet [23], the first end-to-end deep learning method to predict optical flow fields. Sun *et al.* then proposed PWC-Net [24], which uses a coarse-to-fine multiscale approach combined with Cost Volume [25] for multiscale estimation of the optical flow field. Teed *et al.* proposed RAFT [26] to overcome the limitations of coarse-to-fine multiscale methods that do not provide accurate estimates of small displacements. In unsupervised optical flow estimation, Yu *et al.* used STN for unsupervised optical flow [27]. Meister releases UnFlow [28] treats optical flow estimation as an image reconstruction problem. Luo *et al.* proposed UpFlow [29], a novel pyramid structure designed to avoid image damage during downsampling.

III. METHOD

The proposed SearchMorph, as illustrated in Fig. 1. The network aims to refine the deformation field through an iterative approach to register the moving image with the fixed image accurately. Specifically, We input the moving image M and the fixed image F into the feature and context encoder and output the feature map and context. Then we input the feature maps $h(M)$ and $h(F)$ into the association layer and calculate the cost volume of the two feature maps. We then pool the last two dimensions of the cost volume to construct a multi-scale correlation pyramid. The deformation field iterator (ϕ Iterator) iterates over the refinement of the deformation field (ϕ) by entering the correlation pyramid and the context. The deformation field ϕ is 2x upsampled to Φ at the last iteration to restore the original map resolution. When back-propagating, M' and F perform a similarity loss calculation \mathcal{L}_{sim} to optimize the weights of the whole network so that M' becomes increasingly similar to F . We will describe each part in detail below.

A. Feature Extractor

Our proposed feature extractor consists of a feature encoder and a context encoder. We use both encoders for feature extraction. The feature encoder extracts the feature map to calculate the correlation, and the context extractor extracts the context for feature information supplementation. The context addresses the problem of the network becoming one-sided due

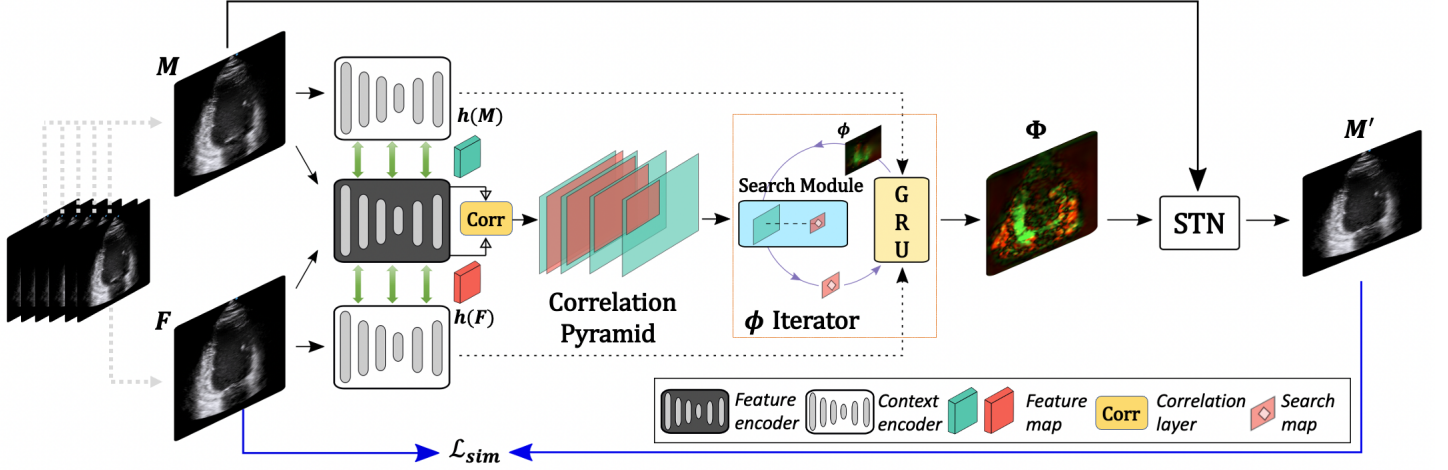


Fig. 1: Overview of SearchMorph for medical image deformation registration. The network consists of four main components, (1) a feature encoder and two context encoders, which share weights; (2) a Correlation layer, which calculates the cost volume between features and constructs the correlation pyramid by pooling; (3) a Deformation field iterator, including GRU and search module, to optimize the deformation field by iteration; (4) STN, Φ warps M by STN to obtain a warped image M' for back propagation, optimizing the whole network.

to the loss of information about the original features caused by calculating correlations.

The feature encoder and the context encoder are similar in structure to U-Net [32], with a skip-connect structure. The last layer of the feature encoder outputs an 8-channel feature map, while the context encoder outputs a 32-channel context. In the feature encoder, we split the feature map of the last layer into two 4-channel feature maps $h(F)$ and $h(M)$ corresponding to the input F and M . Both encoders share weights for each layer except for the last layer. After each convolution, we normalize by Batch normalization and activate with Leaky relu. The exact structure of the feature extractor is shown in the appendix.

B. Correlation Pyramid

We introduce a correlation layer and construct a correlation pyramid. Correlation pyramids can store multi-scale correlation information and play two prominent roles in the network. Firstly, when registering images with complex deformation and low signal-to-noise ratio, the correlation pyramid provides the network with more information about the correlation of features. Secondly, in a subsequent step, the search module can combine multi-scale information for searching, improving the performance of model registration for multi-scale deformations.

The two feature maps are fed into the correlation layer, calculating the cost volume between the feature maps. The inner product of two feature maps can determine the feature correlation, often referred to as the cost volume calculation or affinity calculation. we assume that the two feature maps $h(M) \in \mathbb{R}^{H \times W \times D}$, $h(F) \in \mathbb{R}^{H \times W \times D}$, where H, W is the length and width of the feature map and D is the number of channels of the feature. The correlation between these two

feature maps is calculated as follows:

$$C_{ijkl} = \sum_d h(M)_{i,j,d} \cdot h(F)_{k,l,d} \quad (1)$$

$$C(h(M), h(F)) \in \mathbb{R}^{H \times W \times H \times W} \quad (2)$$

In the above equation, where C denotes the calculation of the correlation of one point. $C(h(M), h(F))$ denotes $h(M), h(F)$ the cost volume of the two feature maps $h(M), h(F)$. d denotes the channel for each pair of points. i, j and k, l denote the coordinates in the moving feature map $h(M)$ and the fixed feature map $h(F)$, respectively. Since $h(M)$ and $h(F)$ are obtained from the same feature encoder, i, j and k, l are in the same coordinate domain. Each pair of feature maps has a correlation volume of $C \in \mathbb{R}^{H \times W \times H \times W}$, where the first two dimensions and the last two dimensions correspond to the Moving image and the Fixed image, respectively.

In the construction of the correlation pyramid, we pool the last two dimensions of $C(h(M), h(F))$ with convolution kernels 1, 2, 4, 8 respectively to obtain four correlation matrices $\{C^0, C^1, C^2, C^3\}$. We refer to these four matrices as the correlation pyramid. The correlation pyramid holds multi-scale information about Fixed Image and serves as a search library for subsequent search modules. In addition, the correlation pyramid retains the high-resolution information from the Moving Image, allowing our model to predict rapidly deforming objects such as echocardiograms.

C. Deformation Field Iterator

This paper proposes a deformation field iterator with two main components, a search module, and a GRU. The search module performs a regional search of the correlation pyramid and outputs a search map. The search map stores information about the points around the point to be registered. GRU simulates the iterative process, which refines the deformation

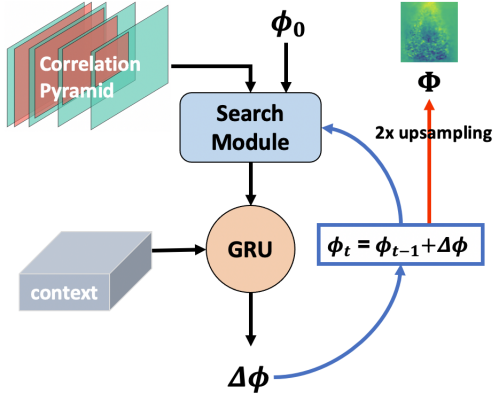


Fig. 2: The figure of the iterative process of the deformation field iterator, ϕ_0 denotes the input deformation field of the first iteration, ϕ_t denotes the deformation field of this iteration, $\Delta\phi$ denotes the field displacement of this iteration, and Φ denotes the final output deformation field. SearchModule outputs the search map based on the correlation pyramid and ϕ_t . GRU outputs $\Delta\phi$ based on the search map and context information.

field through iterations. The search module allows for a clear strategy for model registration, alleviating the problem of unrealistic deformation fields. GRU iteratively refines the deformation field and enables the model to learn helpful information from each iteration. The deformation field iterator gives more detail to the aligned image and makes the deformation field dense and smooth.

The specific iteration steps of the deformation field iterator are shown in Figure 2. For the first iteration, we initialize the deformation field by $\phi_0 = 0$ and then input the correlation pyramid and ϕ_0 into the search module to output the search map. At each iteration, we input the search map and context into the GRU and output a deformation field update operator $\Delta\phi$. We can calculate the deformation field ϕ_t at the output of this iteration based on the update operator. As the iteration proceeds, the registration point gradually converges to a definite point. The deformation field is restored to the original map scale on the last iteration by 2x upsampling.

1) *Search Module*: Suppose that the deformation field calculated in the last iteration is $\phi = (f^x, f^y)$. f represents a matrix. The matrix holds the displacements of the deformation field, f^x and f^y hold the displacements in the x direction and the displacements in the y direction respectively. For a pixel $X = (u, v)$ in the first two dimensions of $C(h(M), h(F))$, warping is performed using ϕ . The distorted pixel is $X^w = (u + f^x(u, v), v + f^y(u, v))$. We construct a set of neighbouring points $\mathcal{P}(X^w)_r$ for X^w :

$$\mathcal{P}(X^w)_r = \{X^w + D \mid D \in \mathbb{Z}^2, \|D\|_1 \leq r\} \quad (3)$$

We take the L1 distance of radius r as the search range of X^w and define the neighborhood $\mathcal{P}(X^w)_r$ of warped points according to this range. The correlation pyramid has four scales $\{C^0, C^1, C^2, C^3\}$. We map X^w to each scale by interpolation, so for each pixel point we have a neighborhood of four scales. A constant radius to search different scales means that we have a larger receptive field in lower scales.

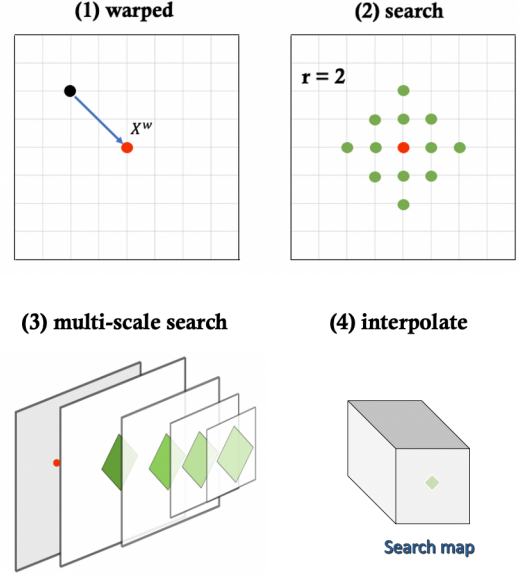


Fig. 3: The search module. There are four steps in total, the first step uses the deformation field to warp the voxel, the second step performs a search range in the warped voxel points, the third step performs a search in the multiscale correlation pyramid, and the fourth step interpolates the multiscale map into a search map. We assume that the deformation field warps the black points to the red point X^w ; the diamond-shaped region consisting of the green points is a search region with a search range of 2 pixels, and all green points are identified as having potential possible matches.

Eventually we concatenate the values of each scale into a feature map, which we call a search map or a motion map. The specific process of the search module is shown in Figure 3.

Theoretically, r should be larger than the maximum deformation value between the two images. We believe that such a search strategy is similar to the diamond block matching method in traditional image processing [35]. The difference is that block matching searches multiple times at the same scale, while this method searches once in each scale within one iteration.

2) *GRU*: The gated recurrent unit (GRU) is a recurrent neural network proposed to solve problems such as long-term memory. In the proposed model, we use the GRU to simulate the iterative recurrent step of a traditional alignment algorithm. GRU can select learning of helpful information in each iteration and allows the network to refine the deformation field multiple times in a single registration without using more parameters. The complete calculation process of GRU is as follows:

$$r_t = \text{sigmoid}(x_t W_{xr} + H_{t-1} W_r + b_r) \quad (4)$$

$$z_t = \text{sigmoid}(x_t W_{xz} + H_{t-1} W_z + b_z) \quad (5)$$

$$\tilde{H}_t = \tanh(x_t W_{hx} + R_t \odot H_{t-1} W_h + b_h) \quad (6)$$

$$H_t = (1 - Z_t) \odot H_{t-1} + Z_t \odot \tilde{H} \quad (7)$$

where x_t denotes the input at the moment t , including the search map and context at the last moment. h_t denotes the

hidden state at moment t , \tilde{h}_t denotes the hidden state of the candidate layer, and Z_t denotes the update gate. The hidden state output by GRU is passed through two convolutional layers to predict the $\Delta\phi$ of the current update of the deformation field. Each iteration produces an update field, $\phi_t = \phi_{t-1} + \Delta\phi$. In the final output, the 2x upsampling deformation field restores it to the original map scale.

D. Spatial transformer layer

Spatial transformer network (STN) [14] is a handy module, the full version of which can be placed in an arbitrary network to accomplish a certain degree of affine transformation, thus improving the predictive performance of the network.

In this paper, we introduce the latter two components of the STN, *Grid generator* and *Sampler*, to warp M . We call the Spatial transformer layer \mathcal{T} . After superimposing the deformed field, the original coordinate system is transformed into a warped image $M^w = T(M, \phi)$ using a bilinear interpolation function. The equation for bilinear interpolation is:

$$\mathcal{T}(M, \phi) = \sum_{q \in \mathcal{N}(p^w)} M(q) \prod_{d \in \{x, y\}} (1 - |p_d^w - p_d|) \quad (8)$$

Where $\mathcal{N}(p^w)$ denotes the warped 8-coordinate neighborhood. d denotes the two-dimensional space. The spatial transformer layer is invertible and does not have to learn any parameters, which can be trained end-to-end by back-propagation during the optimization process.

E. Loss Function

In deformable medical image registration, two steps are usually involved: a rigid transformation for global registration and a non-rigid transformation for local registration. The proposed network does not require a separate rigid transformation to obtain better results. The loss function of this network contains two components, the \mathcal{L}_{sim} similarity loss term and the \mathcal{L}_{reg} deformation field regularity term:

$$\mathcal{L}(M, F, \phi) = \mathcal{L}_{sim}(\mathcal{T}(M, \phi), F) + \alpha \mathcal{L}_{reg}(\phi) \quad (9)$$

Where F denotes a fixed image. M denotes a moving image. ϕ denotes the deformation field of a pair of images. \mathcal{T} represents the deformation, often referred to as *warp* [34] in optical flow networks. In this network, the Spatial transformer layer takes on this part. In summary, \mathcal{L}_{sim} measures how similar the deformed image $\mathcal{T}(M, \phi)$ is to the similarity of the fixed image F , \mathcal{L}_{reg} penalizes the deformation field ϕ to make it smooth. α denotes the strength of the penalty term.

The similarity loss terms we use are mean square error MSE and local normalized cross-correlation $LNCC$. Our experiments found that MSE is more suitable for ultrasound modal images, and $LNCC$ would be more robust for more informative MR images.

The regular term is also known as the smoothing term. We use the most commonly used registration regular term, l2-loss, to penalize the deformation field. The penalized deformation field is smoothed so that the deformed image better matches the texture of the actual image.

IV. EXPERIMENTS

A. Datasets and Preprocessing

We use four datasets to validate the validity of this method. They include a single-temporal brain MR dataset multi-temporal echocardiography dataset. The echocardiographic dataset consists of three different datasets. The details are described as follows:

LPBA40 [33] is a 3d brain MRI dataset. It contains brain MR images from 40 volunteers and is a mono-temporal inter-patient dataset, and we used an atlas-based training strategy to train this dataset. As LPBA40 is 3D data, each of which has the format $160 \times 192 \times 160$ and contains 160 slices, we take the 80th slice of each case for registration in this paper.

CAMUS [36] provides two-dimensional two- and four-chamber echocardiograms of five hundred patients, each with at least one entire cardiac cycle. This dataset provides manual labels for myocardial and cardiac blood pools at the end-diastolic ED and end-systolic ES, which we supplement with labels for the entire sequence.

Synthetic ground-truth data [31] provides 105 sequence videos of A2C, A3C, and A4C with manual labels of the myocardial. We used the A3C in this dataset to compensate for the lack of three-chamber data and provide the cardiac blood pool as additional labels.

Echocardiography Video is the data we acquired. This dataset contains 20 patients, each containing at least two complete cardiac cycles, and we provide manual labels of the myocardial and cardiac blood pools for each frame.

B. Metrics

We use two metrics to assess the registration capability of the model. Dice and the percentage of non-positive values indeterminant of the Jacobian matrix on the deformation field, which we usually refer to as the ratio of the folding points (RFP). A lower Dice index indicates better model performance. The RFP is the ratio of folding points to all voxel points in the deformation field and is a measure of the fidelity of the deformation field. The lower the folding point ratio, the closer the deformation field is to the diffeomorphism.

C. Implementation

To compare model performance fairly, we used the learning rate of 1×10^{-3} and the *Adam* optimizer to update the weights in the neural network for each network. We set α in MSE as 0.01 and α in NCC as 2. During the training, we set the optimization step of each data as 1500 *epoch* and *batchsize* as 8. We set the brain MR image size to 192×160 and echocardiogram image size to 160×160 . In the brain MR registration experiment, we set the search range R of the model in this paper as 3. In the echocardiography experiment, we set R as 2. We set the number of iterations of the deformation field iterator to 4

We have implemented all models on a Linux system with an Intel i7-11700K@3.60GHz x 16 processor and an NVIDIA GeForce RTX 3090 graphics card. The running environment was python version 3.7.11 and the PyTorch 1.8.0 framework, with Cuda version 11.1.1.

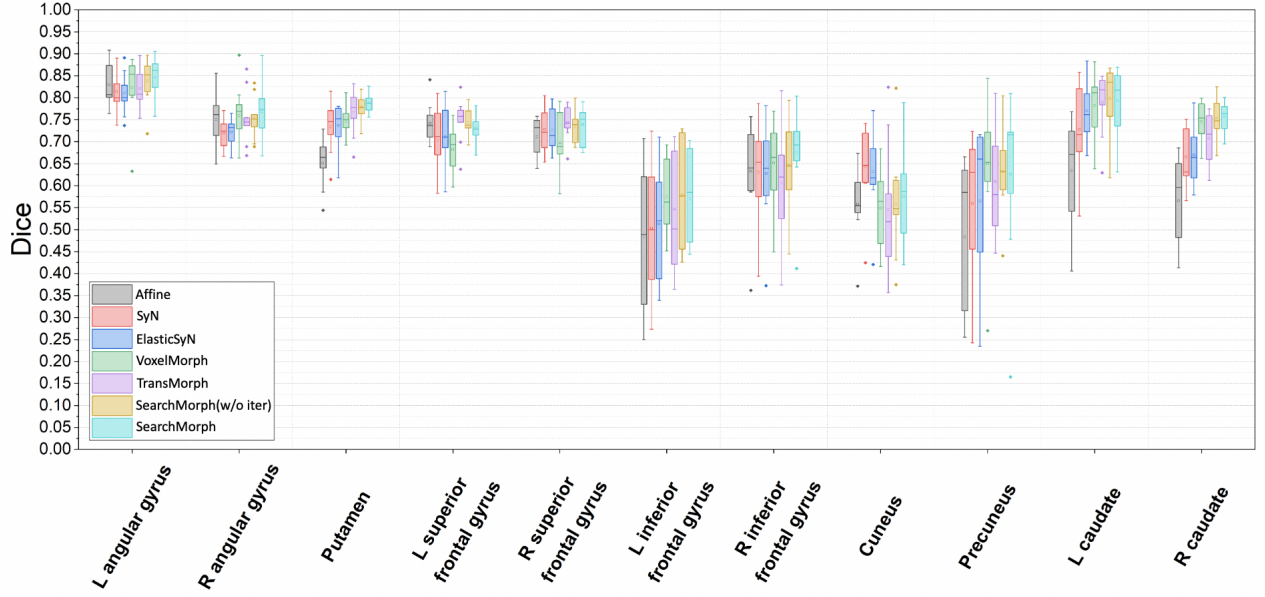


Fig. 4: Brain multi-structure box line diagram. For quantitative evaluation of the registration ability of this paper’s model and Baseline model for LPBA multi-structure, the Dice metric on the vertical axis and the multi-structure names on the horizontal axis, and the legend in the bottom left corner illustrating the method represented by each color.

TABLE I: The table shows the quantitative evaluation results of the LPBA brain MR slice registration. We use the average Dice index and the percentage of non-positive values in the determinant of the Jacobian matrix on the deformation field (% of $|J_\phi| \leq 0$) for evaluation. The numbers in parentheses are the standard deviation between multiple data, reflecting registration stability. Bold indicates the highest score. SearchMorph(w/o iter) indicates the version of this model without iterations, and SearchMorph indicates the version of this model with four iterations.

Model	Dice	% of $ J_\phi \leq 0$
Affine	0.640(0.032)	-
SyN	0.675(0.039)	0.442(0.016)
ElasticSyN	0.680(0.033)	0.428(0.014)
VoxelMorph	0.718(0.017)	0.017(0.004)
TransMorph	0.709(0.028)	0.020(0.004)
SearchMorph(w/o iter)	0.723(0.016)	0.016(0.003)
SearchMorph	0.727(0.020)	0.016(0.003)

D. Comparative experiments

We have compared five state-of-the-art methods in registration tasks, as the baseline, with our proposed model. The baseline includes three traditional methods, Affine, SyN by Advanced Normalization [9], ElasticSyN and two deep learning methods, VoxelMorph [18], Transmorph [19]. In the experiments, SearchMorph(w/o iter) denotes the proposed model without iteration, and SearchMorph denotes the proposed model with four iterations. We validated the performance of the models using the brain MR dataset and the echocardiography dataset.

1) *Single-temporal Brain MR Registration*: Table I shows the quantitative results between the proposed method SearchMorph and the comparison method. As seen from the table SearchMorph and SearchMorph(w/o iter) achieved the highest Dice score of 0.727 and the next highest Dice score of 0.723, respectively. This result indicates that this method has higher registration accuracy than the other methods, and the model

performance is further improved after adding iterations. In addition, our method also achieved the lowest percentage of negative Jacobi determinants of 0.016, proving that our method’s deformation field is smoother and does not sacrifice the realism of the deformation field after adding iterations. Figure 4 shows the box line diagram of the results of the multi-structural registration of brain MR, which contains the registration information of our model with the Baseline model for 11 critical structures such as Cuneus and Precuneus. As seen from the box line plot, SearchMorph scores higher than other models in several structures and has higher stability and upper limits. In particular, SearchMorph excels in the Caudate nucleus and Angular gyrus. Since different structures have different sizes, the box line diagrams’ results fully demonstrate the model’s excellent performance in registering both large and small deformations. Figure 5 shows an example of brain MR registration, where we compare the registration images of the proposed method and the baseline method. In the figure, it can be seen that the SearchMorph-registered images are morphologically closer to the fixed images. To more clearly demonstrate the disparity between the methods in this paper and others, we have boxed the Lateral ventricle and Caudate nucleus in blue boxes and the Subfrontal gyrus in red boxes. In the figure, SearchMorph is closer in shape to the Fix image at the Lateral ventricle and Caudate nucleus. At the lower frontal gyrus, VoxelMorph deformation has apparent incorrectness, and TranMorph has a significant defect. SearchMorph, on the other hand, not only deforms correctly but also makes up for some defects after adding iterations.

2) *Multi-temporal Echocardiogram registration*: The echocardiogram registration experiments evaluate the model’s ability to register multi-temporal and ultrasound modality data with many artifacts. The data used in this experiment include two-chamber, four-chamber CAMUS,

TABLE II: The table shows the results of the quantitative assessment of echocardiographic registration, and we used cardiac blood Dice and myocardial Dice as assessment metrics. The types of data evaluated include echocardiograms of 2CH, 3CH, and 4CH. Standard deviations are in parentheses. Bold indicates the highest score.

Model	2CH		3CH		4CH	
	Blood pool Dice	Myocardial Dice	Blood pool Dice	Myocardial Dice	Blood pool Dice	Myocardial Dice
Affine	0.823(0.107)	0.755(0.121)	0.851(0.048)	0.762(0.146)	0.846(0.089)	0.736(0.140)
SyN	0.876(0.094)	0.797(0.110)	0.900(0.038)	0.800(0.125)	0.876(0.080)	0.781(0.125)
ElasticSyN	0.875(0.096)	0.796(0.111)	0.901(0.035)	0.802(0.120)	0.877(0.080)	0.781(0.125)
VoxelMorph	0.879(0.112)	0.871(0.146)	0.914(0.022)	0.906(0.030)	0.905(0.075)	0.876(0.120)
TransMorph	0.881(0.114)	0.873(0.148)	0.913(0.085)	0.880(0.127)	0.910(0.080)	0.881(0.129)
SearchMorph	0.888(0.112)	0.880(0.142)	0.921(0.021)	0.914(0.028)	0.919(0.068)	0.891(0.113)

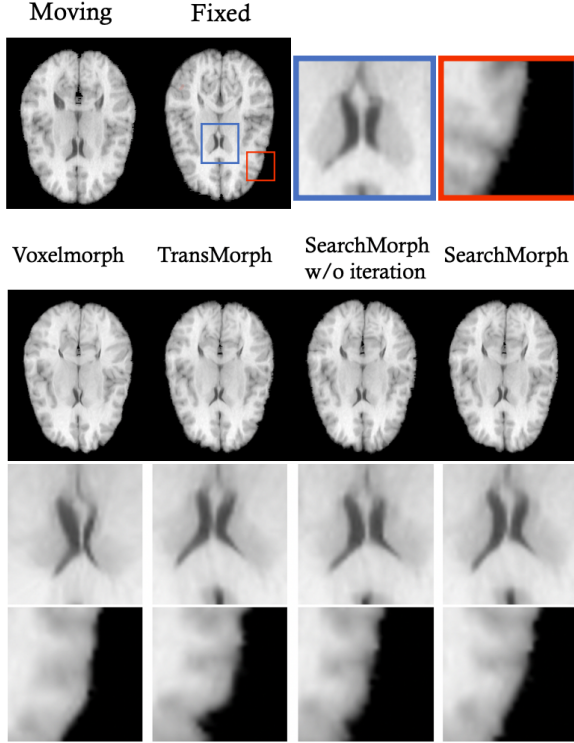


Fig. 5: Example of LPBA brain MR slice registration. The blue box outlines the Lateral ventricle and Caudate nucleus, and the red box outlines the Subfrontal gyrus. The first row shows the moving image, fixed image, and fixed images in the blue and red boxes, the second row shows the results of image deformation for the four registration methods. The third and fourth rows show enlarged views of the four methods in the blue and red boxes, respectively.

three-chamber Synthetic, and our acquisition of two-chamber echocardiograms for a total of 1636 frames in 80 cases. We compare the registration performance of the Dice assessment model for myocardial and cardiac blood pools for this data.

Table II demonstrates the performance of proposed and baseline methods when registering the echocardiogram. We used the left ventricular cardiac blood pool DICE and myocardial DICE as evaluation metrics, and the size of the left ventricle varied in the echocardiography of the different chambers. The table shows that SearchMorph had the highest cardiac blood pool and myocardial Dice in two-chamber, three-chamber, and four-chamber echocardiograms. The experimental results demonstrate that the method in this paper can adapt to multi-scale deformation and shows excellent performance

in the registration of echocardiography with multiple cavity hearts.

Figure 6 demonstrates the echocardiographic systolic registration. The Fixed image is a sequence of two-chamber echocardiograms, where $T=12$ is the image of the left ventricle at end-systole, and the Moving Image is the image of the left ventricle at end-diastole. We marked the ground truth of the endocardium as gray and compared it with the model-registered images to observe the registration effect. VoxelMorph and SearchMorph registrations are better during the first few frames, and TransMorph shows minor deviations. From the sixth frame onwards, the VoxelMorph and TransMorph registered images deviate significantly from the Fixed image, as shown in the red boxed area. VoxelMorph has a better registration of the inner membrane but is defective due to excessive registration deformation, and the endocardial of TransMorph-registered images do not fit the ground truth. The most significant deviations occur when registering the ES frame. Only the SearchMorph-registered echocardiographic sequence was highly overlapping with the endocardial ground truth. The experimental results demonstrate that our model performs best when registering echocardiograms, primarily when registering large deformations showing excellent performance.

In the last column, we show the deformation field for the three methods, red for moving to the right, green for moving to the left, and the shade of the color represents the distance moved. The echocardiogram shown is in systole, with its left wall moving to the right and its right wall moving to the left. As seen in the figure, the deformation field of VoxelMorph registration is almost haphazard, indicating that VoxelMorph does not have a clear strategy when registering. The TransMorph-registered deformation field exhibits a direction of motion that generally conforms to the pattern of cardiac contraction, but its deformation field shows deformation spillover. The spillover manifests in a large red area on the left side that extends beyond the myocardial wall. The TransMorph-registered deformation field also has a red area on the right side, representing a significant deformation estimation error. SearchMorph produces a deformation field consistent with the contraction motion, and the deformation field is smoother and more accurately estimated.

E. Ablation experiments

As seen in Table III, the model's performance decreases with removing any of the components in this model. The

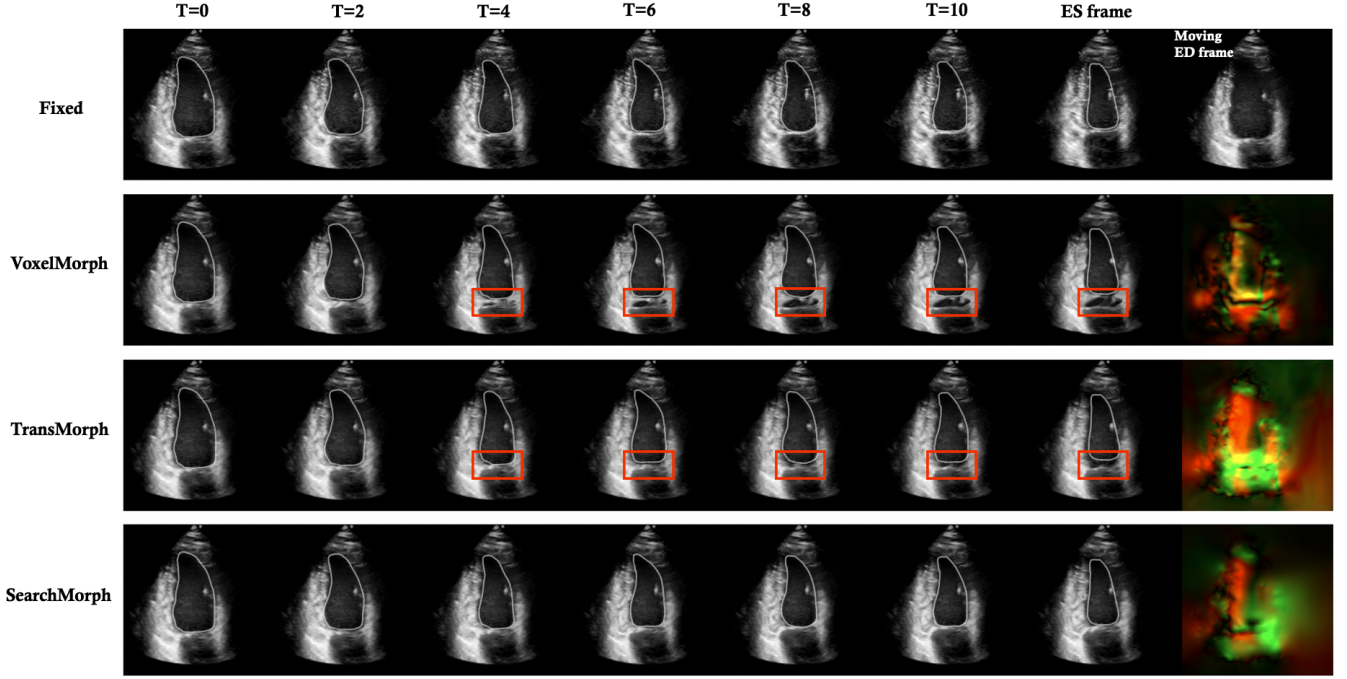


Fig. 6: The effect of registration of each model in the systolic sequence of two-chamber echocardiography is shown. $t=n$ indicates the n th frame, Moving is the ED frame, and $T=12$ is the ES frame. Groundtruth with endocardium marked in gray. We frame in red the areas where the registration image deviates significantly from the Fixed image. The first row shows Fixed sequence images and the Moving image. The second, third, and fourth rows represent VoxelMorph, TransMorph, and SearchMorph aligned echocardiograms, respectively, and their last column shows the deformation fields resulting from the registration of end-diastolic images with end-systolic images.

Dice metrics of the cardiac blood pool and myocardium decrease when the context encoder is removed. When not using correlation calculations, the network outputs the deformation field directly through the features with Blood pool Dice and Myocardial Dice of 0.900 and 0.875, respectively. There is a slight decrease in performance when not using a multi-scale pyramid and only using single-scale feature information for the iterative search. The addition of iteration improves the metric by only 0.004, but in the qualitative analysis above, we found that iteration is evident and necessary for optimizing tiny sites.

Based on the above analysis, we can conclude that our proposed structure allows for better feature extraction for echocardiography. After the model calculates the correlation, there will inevitably be some loss of feature information, and the information obtained from the contextual encoder is particularly critical at this point. The last three ablation experiments illustrate the effectiveness of the network proposed in this paper one by one. Specifically, we will explain why in the discussion.

V. DISCUSSION

1) *Brain MR Registration*: SearchMorph achieved the highest average Dice and the lowest Jacobi determinant non-negative ratio in single-temporal brain MR experiments. SearchMorph not only shows excellent performance in registering multiple structures in the brain but also optimizes more registration details after adding iterations. We analyze this for two important reasons. (1) We designed the deformation field iterator to perform iterative alignment in one prediction. The registration points converge gradually to a definite point. So

the deformation field gradually approaches the actual value after adding iterations, optimizing more registration details. (2) Our model does not sacrifice the realism of the deformation field while gaining from iteration since we add the search module to the deformation field iterator. The search module searches for optimal registration points in a fixed radius, which primarily suppresses the voxel point folding. (3) We use the GRU module to complete the iterative process. GRU allows the model to learn helpful information selectively during the iterations and continuously refine the deformation field, which plays a vital role in this model.

2) *Multi-temporal Echocardiogram registration*: In multi-temporal echocardiographic experiments, SearchMorph performs best in two-chamber, three-chamber, and four-chamber hearts. The experimental results demonstrate the strong capability of the present model in registering multi-scale deformations. The model fits best to the Ground-truth of the myocardial endocardium when registering the systolic two-chamber echocardiogram, which demonstrates the ability of the model to register images with large deformations. We analyze this for three important reasons. (1) This model uses correlation pyramids as the search library for registration, which complements the multi-scale correlation information and enhances the ability of the network to register multi-scale deformations. (2) Due to the characteristics of low signal-to-noise ratio and many artifacts in ultrasound images, it is hard to register the ultrasound images by conventional methods accurately. This strategy mitigates the interference caused by noise in feature extraction. (3) The search module designed in this paper searches the correlation pyramid in a fixed radius,

TABLE III: The table shows the results of the ablation experiments, where we evaluated the contribution of context, search module, correlation pyramid and iteration to the model registration performance using brain MR data, and we used the mean Dice and the percentage of non-positive values in the determinant of the Jacobian matrix as an evaluation metric. Standard deviations are shown in parentheses.

Model	Dice	% of $ J_\phi \leq 0$
w/o context	0.698(0.030)	0.016(0.003)
w/o Search Module	0.722(0.017)	0.020(0.005)
w/o Corr Pyramid	0.705(0.028)	0.015(0.002)
w/o Iteration	0.723(0.016)	0.016(0.003)
SearchMorph	0.727(0.020)	0.016(0.003)

ensuring that the module’s search is small to large. This strategy ensures that the model can register accurately for large deformations at low resolutions.

3) *Ablation experiments*: The ablation experiments’ results demonstrate that this model’s structure contributes to the improvement of the registration performance. We will analyze the reasons for this in detail below. (1) In the ablation experiments of context networks, removing context information causes a decrease in the Dice score of the network. We believe that the context feature information can mutually complement the correlation information to improve the registration performance of the model, which is consistent with our original intent of adding context. (2) After removing the search module, the Dice score decreases, and the percentage of non-positive values in the Jacobian determinant increases. The reason is that the search module can register them by searching for the most relevant points in the region. A reasonable search strategy enables the model to improve performance while suppressing the folding of registration points. (3) After removing the correlation pyramid, the performance of the model decreases significantly. We believe this is because the feature pyramid incorporates multi-scale information that allows the network to be registered to multiple morphologies. The morphology in the brain MR data set is complex, and the correlation pyramids play a vital role in the registration. (4) After removing iterations, the Dice value of the model decreases to some extent. Although its decrease is not significant, it can be found in the qualitative experiments of brain MR that the model after adding iterations gradually converges to the correct value, optimizing the details of the images.

4) *Limitations*: The network proposed in this paper has some limitations. (1) Due to GPU memory limitations, the feature encoder in this paper only upsamples to 1/2 of the original image scale. A lower resolution will affect the registration to some extent. (2) The search strategy proposed in this paper is limited to two-dimensional data. In future work, we expect to design a three-dimensional search strategy adapted to three-dimensional images. (3) The proposed model, while maintaining a low folding point ratio, falls short of differential homozygosity. In subsequent work, we will design a diffeomorphic version of SearchMorph.

VI. CONCLUSION

There is a gradually growing consensus that it is difficult to register images with only one inference. Improving the

registration performance through iteration has become a tough hot spot in registration research. We propose an unsupervised multi-scale correlation iterative registration network, SearchMorph. SearchMorph establishes links between features by calculating the cost volume between features and refining the deformation field in a deformation field iterator. We have also designed a search module that registers voxel points to their surrounding similarities. The experimental results demonstrate that the proposed model exhibits excellent performance in both single-temporal MR and multi-temporal ultrasound images and possesses a lower folding point ratio.

REFERENCES

- [1] D. Rueckert, L. I. Sonoda, C. Hayes, D. L. Hill, M. O. Leach, and D. J. Hawkes, “Nonrigid registration using free-form deformation: Application to breast mr images,” *IEEE Transactions on Medical Imaging*, vol. 18, no. 8, pp. 712–721, 1999.
- [2] D. Shen and C. Davatzikos, “Hammer: Hierarchical attribute matching mechanism for elastic registration,” *IEEE Transactions on Medical Imaging*, vol. 21, no. 11, pp. 1421–1439, 2002.
- [3] R. Bajcsy and S. Kovacic, “Multiresolution elastic matching,” *Computer Vision, Graphics, and Image Processing*, vol. 46, pp. 1–21, 1989.
- [4] Beg, M. Faisal, et al. “Computing large deformation metric mappings via geodesic flows of diffeomorphisms.” *International journal of computer vision* 61.2 (2005): 139-157.
- [5] Shen Z, Vialard F X, Niethammer M. Region-specific diffeomorphic metric mapping[J]. *Advances in Neural Information Processing Systems*, 2019, 32.
- [6] J. Krebs, T. Mansi, H. Delingette, L. Zhang, F. C. Ghesu, S. Miao, A. K. Maier, N. Ayache, R. Liao, and A. Kamen, “Robust non-rigid registration through agent-based action learning,” in *International Conference on Medical Image Computing and Computer-Assisted Intervention (MICCAI)*. Springer, 2017, pp. 344–352.
- [7] H. Sokooti, B. de Vos, F. Berendsen, B. P. Lelieveldt, I. Išgum, and M. Staring, “Nonrigid image registration using multi-scale 3d convolutional neural networks,” in *International Conference on Medical Image Computing and Computer-Assisted Intervention (MICCAI)*. Springer, 2017, pp. 232–239.
- [8] X. Yang, R. Kwitt, M. Styner, and M. Niethammer, “Quicksilver: Fast predictive image registration—a deep learning approach,” *NeuroImage*, vol. 158, pp. 378–396, 2017.
- [9] B. B. Avants, C. L. Epstein, M. Grossman, and J. C. Gee, “Symmetric diffeomorphic image registration with cross-correlation: evaluating automated labeling of elderly and neurodegenerative brain,” *Medical image analysis*, vol. 12, no. 1, pp. 26–41, 2008.
- [10] X. Cao, J. Yang, J. Zhang, D. Nie, M. Kim, Q. Wang, and D. Shen, “Deformable image registration based on similarity-steered cnn regression,” in *International Conference on Medical Image Computing and Computer-Assisted Intervention*. Springer, 2017, pp. 300–308.
- [11] J. Krebs, T. Mansi, H. Delingette, L. Zhang, F. C. Ghesu, S. Miao, A. K. Maier, N. Ayache, R. Liao, and A. Kamen, “Robust non-rigid registration through agent-based action learning,” in *International Conference on Medical Image Computing and Computer-Assisted Intervention (MICCAI)*. Springer, 2017, pp. 344–352.
- [12] Rohé, Marc-Michel, et al. “SVF-Net: learning deformable image registration using shape matching.” *International conference on medical image computing and computer-assisted intervention*. Springer, Cham, 2017.
- [13] H. Sokooti, B. de Vos, F. Berendsen, B. P. Lelieveldt, I. Išgum, and M. Staring, “Nonrigid image registration using multi-scale 3d convolutional neural networks,” in *International Conference on Medical Image Computing and Computer-Assisted Intervention (MICCAI)*. Springer, 2017, pp. 232–239.
- [14] M. Jaderberg, K. Simonyan, and A. Zisserman, “Spatial transformer networks,” in *Advances in neural information processing systems*, 2015, pp. 2017–2025.
- [15] B. D. de Vos, F. F. Berendsen, M. A. Viergever, M. Staring, and I. Išgum, “End-to-end unsupervised deformable image registration with a convolutional neural network,” in *Deep Learning in Medical Image Analysis and Multimodal Learning for Clinical Decision Support*, 2017, pp. 204–212.

- [16] Zhu W, Huang Y, Vannan M A, et al. Neural multi-scale self-supervised registration for echocardiogram dense tracking[J]. arXiv preprint arXiv:1906.07357, 2019.
- [17] Qin C, Bai W, Schlemper J, et al. Joint learning of motion estimation and segmentation for cardiac MR image sequences[C]//International Conference on Medical Image Computing and Computer-Assisted Intervention. Springer, Cham, 2018: 472-480.
- [18] Balakrishnan G, Zhao A, Sabuncu M R, et al. An unsupervised learning model for deformable medical image registration[C]//Proceedings of the IEEE conference on computer vision and pattern recognition. 2018: 9252-9260.
- [19] Chen J, Du Y, He Y, et al. TransMorph: Transformer for unsupervised medical image registration[J]. arXiv preprint arXiv:2111.10480, 2021.
- [20] Zhao S, Dong Y, Chang E I, et al. Recursive cascaded networks for unsupervised medical image registration[C]//Proceedings of the IEEE/CVF International Conference on Computer Vision. 2019: 10600-10610.
- [21] Fan J, Cao X, Xue Z, Yap P T and Shen D 2018 Adversarial similarity network for evaluating image alignment in deep learning based registration Int. Conf. Medical Image Computing and Computer-Assisted Intervention (Berlin: Springer) pp 739–46
- [22] Kim B, Kim D H, Park S H, et al. CycleMorph: cycle consistent unsupervised deformable image registration[J]. Medical Image Analysis, 2021, 71: 102036.
- [23] Dosovitskiy A, Fischer P, Ilg E, et al. Flownet: Learning optical flow with convolutional networks[C]//Proceedings of the IEEE international conference on computer vision. 2015: 2758-2766.
- [24] Sun D, Yang X, Liu M Y, et al. Models matter, so does training: An empirical study of cnns for optical flow estimation[J]. IEEE transactions on pattern analysis and machine intelligence, 2019, 42(6): 1408-1423.
- [25] A. Hosni, C. Rhemann, M. Bleyer, C. Rother, and M. Gelautz, "Fast cost-volume filtering for visual correspondence and beyond," IEEE Transactions on Pattern Analysis and Machine Intelligence (TPAMI), 2013.
- [26] Teed Z, Deng J. Raft: Recurrent all-pairs field transforms for optical flow[C]//European conference on computer vision. Springer, Cham, 2020: 402-419.
- [27] Yu J J, Harley A W, Derpanis K G. Back to basics: Unsupervised learning of optical flow via brightness constancy and motion smoothness[C]//European Conference on Computer Vision. Springer, Cham, 2016: 3-10.
- [28] Meister S, Hur J, Roth S. Unflow: Unsupervised learning of optical flow with a bidirectional census loss[C]//Proceedings of the AAAI conference on artificial intelligence. 2018, 32(1).
- [29] Luo K, Wang C, Liu S, et al. Upflow: Upsampling pyramid for unsupervised optical flow learning[C]//Proceedings of the IEEE/CVF Conference on Computer Vision and Pattern Recognition. 2021: 1045-1054.
- [30] Luo K, Wang C, Liu S, et al. Upflow: Upsampling pyramid for unsupervised optical flow learning[C]//Proceedings of the IEEE/CVF Conference on Computer Vision and Pattern Recognition. 2021: 1045-1054.
- [31] Alessandrini M, Chakraborty B, Heyde B, et al. Realistic vendor-specific synthetic ultrasound data for quality assurance of 2-D speckle tracking echocardiography: simulation pipeline and open access database[J]. IEEE transactions on ultrasonics, ferroelectrics, and frequency control, 2017, 65(3): 411-422. Access Database.
- [32] Ronneberger O, Fischer P, Brox T. U-net: Convolutional networks for biomedical image segmentation[C]//International Conference on Medical image computing and computer-assisted intervention. Springer, Cham, 2015: 234-241.
- [33] Shattuck D W, Mirza M, Adisetiyo V, et al. Construction of a 3D probabilistic atlas of human cortical structures[J]. Neuroimage, 2008, 39(3): 1064-1080.
- [34] T. Brox, A. Bruhn, N. Papenberg, and J. Weickert. High accuracy optical flow estimation based on a theory for warping. In ECCV, volume 3024, pages 25–36. Springer, 2004. 2
- [35] Zhu S, Ma K K. A new diamond search algorithm for fast block-matching motion estimation[J]. IEEE transactions on Image Processing, 2000, 9(2): 287-290.
- [36] S. Leclerc, E. Smistad, J. Pedrosa, A. Ostvik, et al. "Deep Learning for Segmentation using an Open Large-Scale Dataset in 2D Echocardiography" in IEEE Transactions on Medical Imaging, early access, 2019